

Ion Impacts on Graphene/Ir(111): Interface Channeling, Vacancy Funnels, and a Nanomesh

Sebastian Standop,^{*,†} Ossi Lehtinen,^{‡,§} Charlotte Herbig,[†] Georgia Lewes-Malandrakis,[†] Fabian Craes,[†] Jani Kotakoski,^{‡,||} Thomas Michely,[†] Arkady V. Krashennnikov,^{‡,⊥} and Carsten Busse[†]

[†]II. Physikalisches Institut, Universität zu Köln, Zùlpicher Straße 77, 50937 Köln, Germany

[‡]Department of Physics, University of Helsinki, P.O. Box 43, 00014 Helsinki, Finland

[§]Central Facility for Electron Microscopy, Group of Electron Microscopy of Materials Science, University of Ulm, 89081 Ulm, Germany

^{||}Department of Physics, University of Vienna, Boltzmanngasse 5, 1190 Wien, Austria

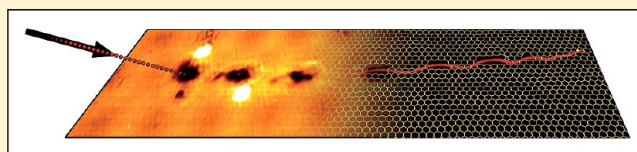
[⊥]Department of Applied Physics, Aalto University, P.O. Box 11100, 00076 Aalto, Finland

Supporting Information

ABSTRACT: By combining ion beam experiments and atomistic simulations we study the production of defects in graphene on Ir(111) under grazing incidence of low energy Xe ions. We demonstrate that the ions are channeled in between graphene and the substrate, giving rise to chains of vacancy clusters with their edges bending down toward the substrate.

These clusters self-organize to a graphene nanomesh via thermally activated diffusion as their formation energy varies within the graphene moiré supercell.

KEYWORDS: Graphene, ion-bombardment, self-organization, STM, MD, DFT



Ion beam irradiation is a powerful tool for the creation of nanostructured surfaces.¹ Often even regular patterns appear spontaneously, thereby constituting a prominent example of self-organization.² Ion bombardment can also be used to tailor the properties of nanoscale materials, including graphene.^{3,4} It is therefore tempting to explore the possibilities of using ion beams for the creation of nanostructures in supported graphene with the desired properties, such as arrays of graphene nanoislands,⁵ nanoribbons,⁶ and hole or antidot lattices (also called nanomesh).⁷ The latter structure has been predicted to cause bandgap opening at the Fermi level due to spatial confinement of electrons, offering a way to tune the electronic⁸ and thermoelectric properties⁹ of graphene-based devices. Furthermore, certain hole arrangements are predicted to induce magnetism in the patterned graphene sheet¹⁰ which should have an impact on spin transport properties. The nanomesh structure may also be applied as a template for patterned adsorption. However, in spite of considerable success in nanostructuring graphene by plasma treatment through a nanoporous membrane,¹¹ etching of graphene devices by a 30 keV He ion beam,¹² or cutting of graphene by swift heavy ions,¹³ no experiment has yet exploited ion beams for pattern formation in graphene.

Although recent transmission electron microscopy (TEM) experiments have provided lots of insight into the structure and dynamics of point defects in graphene,^{14,15} one can only study defect formation and evolution induced by the electron beam itself. Besides, applying this technique to graphene on metals is much more challenging due to a weak contrast of carbon atoms

as compared to the much heavier metal atoms. Meanwhile, scanning tunneling microscopy (STM) studies on supported graphene bombarded with low energy ions^{16–18} made it possible to obtain direct information on the irradiation-induced defects. For graphene on Pt(111) localized states at the Fermi energy resulting from dangling carbon bonds were detected.¹⁷ These electronic signatures of vacancies in graphene were significantly affected by the substrate, which indicates that the vacancy structure is different from the one in free-standing graphene and calls upon further studies. Also these studies leave the annealing behavior of vacancy defects in graphene unexplored.

In this work, using STM we study defect patterns in graphene on an Ir(111) support which appeared due to keV ion bombardment and elucidate the formation mechanism of these patterns using molecular dynamics (MD) simulations. We employ noble gas ions under grazing incidence to maximize the interaction of the ions with graphene. Low fluences are chosen to make the damage patterns of individual ions visible. Furthermore we study the thermal stability of defects. Combining our experiments and density functional theory (DFT) calculations, we show that, with the onset of vacancy cluster mobility around 800 K, the vacancies sense formation energy differences within the moiré supercell formed by the graphene layer with the incommensurate Ir metal substrate.

Received: December 18, 2012

Revised: April 5, 2013

These formation energy differences are exploited to form a graphene nanomesh on Ir(111).

Our experiments were performed in an ultrahigh vacuum system (base pressure $p < 1 \times 10^{-10}$ mbar). We prepared the substrate by cycles of 5 keV Xe⁺ bombardment and flashing to 1400 K. Graphene was then grown from ethylene (C₂H₄) up to full monolayer coverage utilizing a combination of temperature programmed growth (TPG, with temperature of adsorption $T_{\text{ads}} = 300$ K, heating temperature $T_{\text{heat}} = 1350$ K) and chemical vapor deposition (CVD) at $T_{\text{CVD}} = 1125$ K.¹⁹ For both preparation of the substrate and irradiation of graphene, ion bombardment was performed under $(75 \pm 1)^\circ$ with respect to the surface normal along the close-packed $[1\bar{1}0]_{\text{Ir}}$ direction (within $\pm 2^\circ$) of the Ir surface. The ion fluence is smaller than 20 eV. The ion fluence is given in MLE [MLE = monolayer equivalent, 1 MLE corresponds to the surface atomic density of Ir(111), i.e. 1.57×10^{19} particles/m²]. The fluence was measured by a Faraday cup and additionally calibrated by counting the number of (well separated) defect patterns under conditions where each ion leads to significant damage.^{20,21} The resulting morphologies were analyzed using STM at room temperature. Spectroscopy measurements were performed at 5 K on a sample after 250 eV Ne⁺ bombardment under normal incidence. The software WSxM²² was used for image processing.

Figure 1a shows a topographic image of the fully graphene covered Ir(111) surface after ion bombardment. The typical moiré superstructure of graphene/Ir(111)²³ is visible as a hexagonal lattice of depressions (lattice constant of 2.53 nm). It is due to the different registry of the carbon atoms with respect to the substrate inside the incommensurate supercell [10.32×10.32 graphene cells on 9.32×9.32 Ir(111) cells]. In the TOP region, the carbon ring is centered above an atom of the metal surface, whereas in the HCP (FCC) region, the center of the ring is situated above a 3-fold hollow site of hcp (fcc) type (see inset of Figure 1a for an atomically resolved image and Figure 3 for a model). This varying geometry also leads to differences in binding between the carbon layer and the metal substrate (weaker in the TOP regions, stronger in the HCP/FCC regions²⁴), resulting in electron density modulations which are visible in the STM topographs. We note that while the slight height modulation in the moiré depends on tunneling parameters and tip state²⁵ (the TOP-regions either appear as bright dots in a dark sea—topographic contrast—or as dark dots in a bright sea—reverse contrast), other morphological features in the STM topographs (step heights, depth of holes and protrusions) do not. Unless noted otherwise, all STM topographs are in reverse contrast.

The defect patterns visible in Figure 1a are caused by irradiation with 5 keV Xe⁺ ions impinging 75° off normal. The projection of the primary beam is along the close-packed $[1\bar{1}0]_{\text{Ir}}$ -direction of the iridium substrate as indicated by the white arrows. This is also along the $[1\bar{1}\bar{2}0]_{\text{gr}}$ -direction (zigzag-direction) of the graphene layer due to the epitaxial arrangement and consequently also parallel to the close-packed direction of the moiré pattern. The fluence was set to $F = 0.8 \times 10^{-4}$ MLE. Individual defect patterns (i.e., structures caused by just one ion) can be distinguished. Each one is marked with an arrow in Figure 1a. Note that sometimes the assignment of individual defect patterns is ambiguous.

The majority of the defect patterns extend in the direction of the incident ions, and a single pattern consists of a chain of depressions, often accompanied by bright protrusions. We

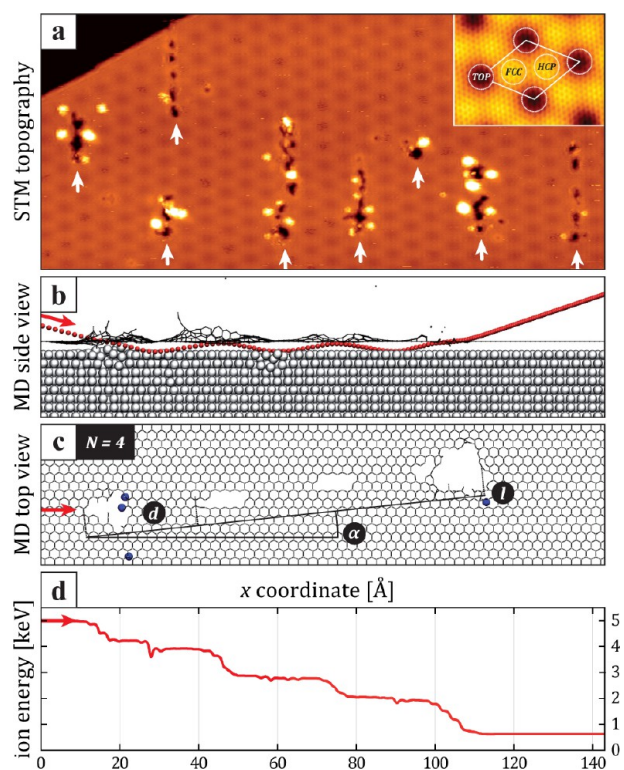


Figure 1. Defect patterns: experiment and MD simulation. (a) STM image of the fully graphene covered Ir(111) surface after room temperature irradiation with 5 keV Xe⁺ ions at 75° off normal, fluence $F = 0.8 \times 10^{-4}$ MLE. Individual defect patterns are marked by arrows pointing along the direction of the impinging ions. A preexisting substrate step is visible in the upper left corner. Inset: Atomically resolved image of the moiré pattern where HCP, FCC, and TOP denote regions of high symmetry. Image width: 53 nm (inset: 6.5 nm); imaging parameters: $I = 0.9$ nA (3.0 nA), $U = 12$ mV (12 mV). (b) Snapshot from a MD simulation showing the side view of a single 5 keV Xe⁺ ion impinging on graphene/Pt(111) at 75° off normal (Xe is impinging from the left). The size of the simulated layer is 8.7 nm \times 22 nm. The time-lapse motion of the ion (red circle) is shown in steps of 2 fs (position of graphene and iridium atoms at simulation time of 170 fs). (c) Top view of the same simulated impact at 1000 fs. For clarity the image shows the resulting graphene layer and metal adatoms (blue spheres) only. The quantities l (length of defect pattern), α (deviation of chain from close-packed row), d (distance between two holes), and N (number of holes) are indicated. (d) Evolution of ion energy during the simulation as the ion travels over the lateral coordinate x for the event shown in b and c.

tentatively interpret the depressions as holes in the graphene layer. The depth of the holes cannot be determined directly as the STM image is a convolution of the sample topography with the STM tip. As shown in Figure S1 of the Supporting Information the tip shape is the dominating effect in the case of small structures investigated here. However, as the apparent depth increases with increasing diameter and saturates for large depressions (see Figure 4d,e) at the distance between the graphene sheet and the metal substrate, the measured topography corroborates our interpretation of the depressions as holes in graphene (see Supporting Information for a detailed discussion). Due to the stochastic nature of damage formation by ion irradiation the quantities characterizing an individual pattern show a broad distribution around their mean values. We defined several measures to characterize the damage patterns; see Table 1. The longest patterns observed have up to nine

Table 1. Quantitative Characterization of the Defect Patterns^a

	exp.	σ	sim.	σ
\bar{N}	2.7	1.8	2.6	1.5
\bar{l} (nm)	8.9	4.2	7.3	4.0
\bar{d} (nm)	2.3	0.9	3.1	1.1
$\bar{\alpha}$ (deg)	1.3	8.9	0.2	6.4

^aComparison of experimental (exp.) and simulation (sim.) results for average values of several measures for the defect patterns induced by ion irradiation, along with their respective standard deviations (σ): average number of holes that can be associated with a single impact \bar{N} , average length of the damage patterns defined as the distance between the first and the last hole of a chain \bar{l} , average distance between two holes \bar{d} , and average angle of the line joining the first and the last hole with respect to the close-packed $[1\bar{1}20]_{\text{gr}}$ direction.

depressions and extend over more than 20 nm. For a fraction of $f_{\text{prot}} = 0.81 \pm 0.02$ of patterns the holes are accompanied by bright protrusions of ≈ 0.2 nm in height.²⁶

To understand the damage formation in detail, we carried out atomistic simulations at the classical MD level of approximation using the PARCAS code.²⁷ We approximate the experimental system by conducting the simulations for graphene on a Pt substrate (Ir's neighbor element in the periodic table, with the same fcc crystal structure) as an interatomic potential is available for Pt–C, but not for Ir–C. Due to the similarity of Pt and Ir, the main conclusions drawn from the simulations are expected to be transferable to the Ir–C system. In the simulations, the Pt–Pt, Pt–C and C–C interactions were modeled using an analytical bond-order potential²⁸ smoothly joined with the universal repulsive Ziegler–Biersack–Littmark (ZBL) potential²⁹ at small atom separations. The Xe–Pt and Xe–C interactions were described by the ZBL potential. As ion energies were quite low, and energy transfer from the projectile to the target atoms was fully governed by nuclear collisions, electronic stopping was not included in the simulations. We used a simulation super cell of 36×79 Pt atoms with a height of 15 layers (42 660 Pt atoms in total). On top of this we placed 40×87 graphene unit cells (6960 C atoms), resulting in a commensurate 11-on-10 structure. The graphene lattice constant was set to 0.252 nm, which is the equilibrium value for the employed interatomic potential. Accordingly the Pt lattice constant had to be slightly increased ($\approx 1\%$) from the equilibrium value of the potential. The graphene-substrate distance was set to the experimental value of 0.338 nm^{24} for the Ir–C system in order to model the experimental conditions. The long-scale height variation of the moiré-pattern was neglected. The simulations were carried out at 0 K with a total simulation time of 1000 fs, which is adequate for the completion of the collision process. Time scales typical for defect diffusion are unreachable by the MD simulations. Nevertheless, due to relatively high migration barriers, most of the defects created by ion impacts will be stable at room temperature. A total of 300 simulations were run, where Xe ions with a kinetic energy of 5 keV impacted the target at 75° with respect to the surface normal along the close-packed $[1\bar{1}0]_{\text{Ir}}$ direction, identical to the experimental setup. The impact points were randomly chosen in the simulated supercell. Statistics on the number and distribution of holes in graphene and adatoms on the metal surface were gathered by counting their numbers and determining their locations at the end of a simulation.

An example of the irradiation simulations is presented in Figure 1b, which shows a time-lapse side view of an impact that caused the formation of $N = 4$ holes and extends over $d = 10.4$ nm. The image illustrates the Xe-ion path (impinging from the left) with red spheres at a time interval of $\Delta t = 2$ ps, revealing an oscillatory motion at the graphene/metal interface: The ion first penetrates the graphene layer after which it is repeatedly reflected at the metal surface and the carbon sheet. The impacts on graphene result in carbon sputtering, causing a track of holes in the graphene layer, clearly visible in the top view of the last frame of the simulation (Figure 1c). The simulated and the experimental impact patterns show qualitative agreement which justifies our assumption that the depressions observed in experiment are indeed holes in the graphene layer. As is obvious from the plot in Figure 1d, the Xe ion loses remarkably more energy upon encounter of graphene as compared with the collisional contact with the Ir(111) surface. This difference originates from a much larger ion to target atom mass ratio for Xe to graphene compared with Xe to the substrate. The averaged results of the simulations are presented along the experimental ones in Table 1, showing a good quantitative agreement without using any fitting parameters. We point out that the experimental and theoretical value for the distance between two holes d is in line with a simple geometrical model of the oscillation period which yields $d = 2h \tan 75^\circ = 2.53 \text{ nm}$, using $h = 0.338 \text{ nm}^{24}$ for the height of the graphene sheet above the metal.

The guided motion of the ion in the interface region is analogous to subsurface channeling observed earlier for the case of pristine crystal surfaces:^{30,31} For the given ion energy and angle, the projectile penetrates the topmost crystal layer and is guided in between this layer and the one underneath parallel to the surface. Consequently the ion is trapped between the layers until it can dechannel after a comparably unlikely scattering event. Our experiments reveal that such a channeling process is also possible at the interface of two different materials. The Ir atoms form perfect strings with respect to the ion beam direction and possess wider shadow cones, causing better overlap as compared to the C atoms. In addition to interface channeling we also observed some cases of subsurface channeling; that is, the ion penetrates the Gr layer and the topmost Ir layer and conducts a channeling motion underneath the Ir(111) surface layer.

Besides supporting our interpretation of the experimental results, the MD simulations also lead to insight not directly accessible via experiment: We find that 34% of the ions are reflected into vacuum upon their first impact to graphene, but still leave significant damage behind. Of the penetrating ions, 41% end up between the graphene and the substrate, while 13.5% are buried in the metal and 45.5% escape into vacuum, penetrating the graphene a second time. The probability for the ion to penetrate the graphene sheet from below is significant (22% per impact). In consequence, only an ion encountering a lucky streak can travel in the interface considerably further than average, explaining the broad distribution of the relevant quantities.

Regarding the sputtering yield of metal atoms, it is decreased in the presence of graphene from $Y_{\text{sub}} = 8.3$ for the pristine surfaces (200 simulations on a Pt target without the graphene layer were conducted in order to obtain this value) to $Y_{\text{sub}} = 0.65$. The sputtering yield for carbon is $Y_{\text{C}} = 17.0$. For the example shown in Figure 1, 27 carbon atoms but zero Pt atoms were sputtered. We also determined the Pt adatom yield by

carrying out a subset of simulations over an extended time (20 ps). We then counted all atoms elevated by more than $0.5 h$ above the metal surface as adatoms, where h is the interlayer spacing of Pt. The adatom yield thus determined is $Y_{\text{ad}} = 33$. It varies significantly between different impacts and is highest for the 19% of events where subsurface channeling takes place.

The fair quantitative agreement between experiment and simulation validates the model of interface channeling. The depressions are identified as holes in the carbon layer. However, their exact atomic structure cannot be determined due to the complexity of the resulting morphologies. In view of the significant adatom yield found in the MD simulations, the bright protrusions are likely to be aggregates of Ir adatoms similar to what has been found for subsurface channeling on Pt(111),³¹ which are buried beneath the graphene sheet in our system. However, a priori we cannot exclude that the bright protrusions result from an enhanced density of states due to dangling carbon bonds^{16,17} or from rearranged carbon atoms. In order to clarify these issues, we next investigated the thermal stability of the defect patterns.

We gradually heated an irradiated sample in steps of 150 K (30 s at each temperature). The resulting topographies at selected temperatures are shown in Figure 2a–c, while the full data set is provided in the diagram of Figure 2g, showing the coverage of defect patterns θ_{pat} (black open circles) as well as the fraction of defect patterns accompanied by protrusions f_{prot} (red closed circles) against annealing temperature T .

At room temperature (Figure 2a), protrusions are present in almost 80% of the defect patterns. As can be seen in Figure 2d, the graphene lattice is continuous across the protrusions, showing that they arise from the interface area below graphene. After annealing to 600 K, protrusions decrease in number while growing in size (Figure 2g). They finally disappear at temperatures close to 750 K.

This annealing behavior is in line with the assumption that the protrusions are due to iridium adatom clusters produced by the ion impact and covered by the graphene sheet: It is known that adatom clusters larger than $n = 4$ are immobile for the case of pristine Ir(111) at room temperature,³³ i.e., the temperature during ion irradiation. We expect that this behavior does not change drastically for the case of adatom clusters between the metal surface and the weakly interacting graphene sheet. Therefore, larger clusters formed either directly by the impact or by agglomeration of smaller clusters should remain stable during the irradiation experiment. In contrast, even rather large clusters ($n \leq 13$) become mobile at elevated temperatures around $T = 500$ K for the case of pristine iridium.³³ This is the same temperature range where the bright protrusions vanish in the experiment. Assuming again that the presence of graphene has only a weak influence on this diffusion process, we can postulate the following mechanism: The clusters diffuse and recombine with the corresponding Ir surface vacancies, leading to their disappearance. Also our MD simulations predict the formation of adatoms at the interface. A remaining discrepancy is the fact that in the simulations the adatoms are mostly found along the ion track, whereas in experiment they are found next to it with a preference for the TOP-regions (see Figure 1a). This can be explained by diffusion of adatoms to the pockets between graphene and the substrate in the TOP regions, which occurs at time scales beyond the reach of MD simulations. Note that for the simulation depicted in Figure 1b–d the adatom yield is low, as no subsurface channeling took place here. The alternative models for the nature of the bright protrusions

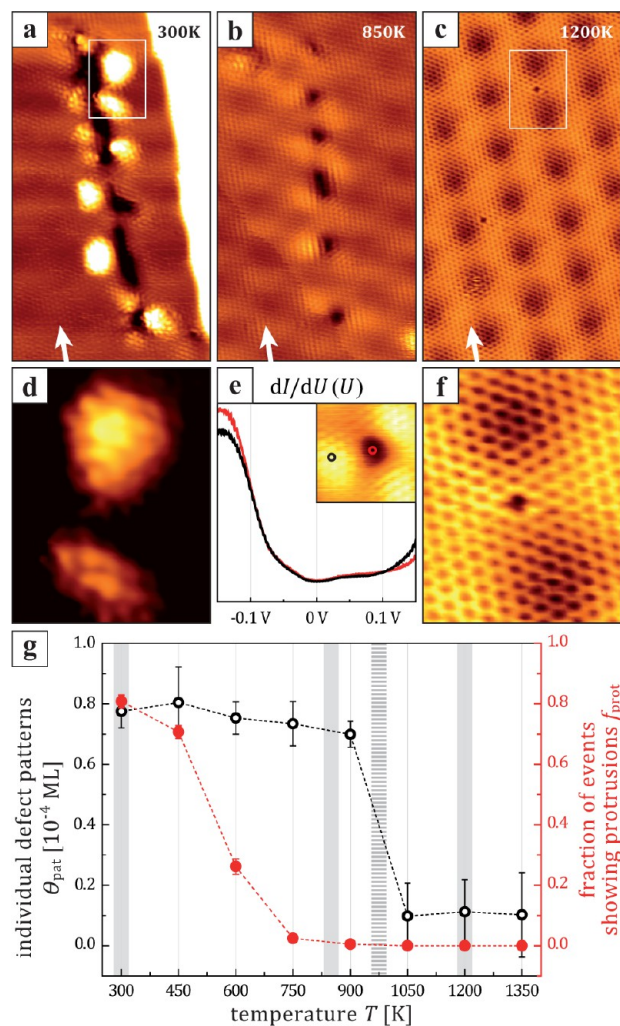


Figure 2. Thermal stability of defects. (a) STM image of the graphene covered Ir(111) surface after $E = 5$ keV Xe^+ bombardment with $F = 0.8 \times 10^{-4}$ MLE, recorded at room temperature. A preexisting substrate step is visible on the right-hand side. (b,c) STM topographs after steps of 30 s annealing at $T = 850$ and 1200 K, respectively (note that a–c are taken at different locations). (d) Bright protrusions after bombardment with atomic resolution. (e) Scanning tunneling spectroscopy measurement on (red line) and next to (black line) a hole in the graphene sheet as indicated in the inset (topographic contrast). (f) Residual defect in atomic resolution. (g) Coverage of defect patterns θ_{pat} (black open circles) and fraction of patterns showing protrusions f_{prot} (red closed circles) plotted against the annealing temperature T . Lines are depicted to guide the eye. Temperatures corresponding to a–c are shaded gray. The dashed vertical line indicates the temperature of the transition from amorphous carbon to graphene (≈ 970 K³²). Arrows in a–c are pointing along the direction of the impinging ions. Image width: (a–c) 9 nm, (d–f) 2.6 nm; imaging parameters: (a,d) $I = 2.2$ nA, $U = 180$ mV; (b) $I = 1.1$ nA, $U = 130$ mV; (c,f) $I = 5.0$ nA, $U = 130$ mV; (e) $I = 0.5$ nA, $U = 470$ mV.

mentioned above can now be excluded: Disordered, amorphous-like regions of carbon only transform into graphene at much higher temperatures (≈ 970 K³²). Also unsaturated carbon bonds offer no sound explanation as the appearance of the protrusions are highly nonuniform, when compared to the modulation patterns observed by Ugeda et al.¹⁶ Furthermore, we often observe holes in the graphene layer without extended protrusions.

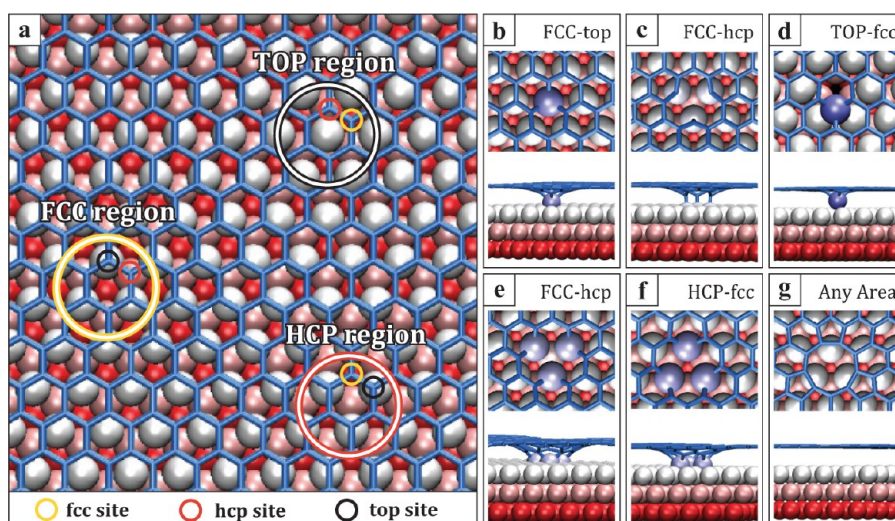


Figure 3. Atomic structure of single and tetra-vacancies in graphene on top of Ir(111) surface as obtained in the DFT calculations. (a) Defect-free surface. Regions of high symmetry (HCP, FCC, TOP region) are indicated by large circles. The sites of selected individual carbon atoms are indicated by colored small circles. Ir atoms are colored according to their elevation. (b–d) Top and side views of a single vacancy in different configurations. (e–g) Top and side view of different tetra-vacancy configurations.

In contrast to the iridium adatom clusters, the vacancy clusters in the graphene sheet remain present at 850 K (Figure 2b). However, their edges appear not very sharp in STM; the holes rather have the shape of funnels reaching down toward the substrate. Since the presence of unsaturated bonds can often be verified by the detection of a peak in the density of states at the Fermi energy, we performed scanning tunneling spectroscopy (STS) on the funnel-shaped holes (Figure 2e). The spectra recorded on intact graphene (black line) and at the hole site (red line) are similar and show a typical shape for graphene on metal surfaces. Specifically, we observe no peak close to 0 V which proves the absence of dangling bonds in our system, in contrast to previous experiments for graphene/Pt(111).¹⁷ These findings of funnel-shaped vacancies and absence of dangling bonds hold for holes of all sizes and shapes.

Finally, the holes also begin to disappear just around 970 K, which is close to the temperature of the transition from amorphous carbon to graphene mentioned before.³² Consequently, at this temperature single vacancies and small vacancy clusters are able to undergo large-scale diffusion. At the highest investigated temperatures ($T \geq 1200$ K, Figure 2c) the graphene layer appears to be entirely rebuilt on a large scale. Specifically, we do not observe larger vacancy islands as a result of defect agglomeration. A possible pathway to lower the energy of the system without the formation of large holes in the graphene is the edge dislocation climb mechanism recently observed by Warner et al.¹⁵ under electron irradiation of graphene. This process can start with a single vacancy which is transformed into a pair of neighboring, opposing edge dislocations. Note that an edge dislocation is a point defect for the case of a 2D material. These defects can be driven apart by dislocation climb upon the incorporation of further vacancies. The graphene lattice in between the dislocations is structurally coherent, but slightly tensile. This mechanism significantly reduces the defect density and leaves very little residual damage behind, in line with our observations. An example of such a residual defect (most probably a double vacancy) is given in Figure 2f. The remaining small defect density can not be estimated to great accuracy, resulting in uncertainties for the case of high temperatures.

By means of our annealing series we now understand the atomic structure of defects. Whereas the protrusions are caused by iridium adatom clusters buried under the graphene layer, the holes correspond to vacancies in the graphene sheet. As the holes appear like a funnel and we do not detect a signal in STS that can be attributed to dangling bonds, we assume that the carbon atoms at the edge of the hole are bound to the metal substrate.

In order to get a microscopic insight into the atomic structure of the vacancy-type defects, we carried out first-principles simulations using DFT as implemented in the plane-wave-basis-set VASP³⁴ code. We used projector augmented wave (PAW) potentials³⁵ to describe the core electrons and two different van der Waals (vdW) functionals^{36,37} for exchange and correlations. The kinetic energy cutoff (400 eV) and k -point sampling over the Brillouin zone ($3 \times 3 \times 1$ mesh) were chosen to guarantee that defect formation energies (for the system studied) are converged within 0.1 eV. This accuracy made it possible to draw all the conclusions, while avoiding excess computational effort. All calculations were carried out for a 200-atom 10×10 graphene supercell on top of a (111) 9×9 Ir slab containing 243 atoms. For the pristine system, we received essentially the same results as in ref 24. We calculated the equilibrium geometries as well as the formation energies of various vacancy configurations, Figure 3 and Table 2. It turned out that for the case of graphene/Ir(111) not only the atomic positions of the carbon atoms in the graphene sheet had to be taken into account but also the relation to the metal atoms underneath. To obtain representative results, we studied several defect configurations corresponding to various positions of vacancies in the moiré pattern.

As defined above, three prominent regions of the moiré pattern can be identified by correlating the position of the carbon hexagon with the atoms of the metal: The very similar, strongly bound HCP- and FCC-regions and the more weakly bound TOP regions. In the HCP-region, three carbon atoms of one graphene hexagon are found in a top site (HCP-top) and three in an fcc site (HCP-fcc). In a similar manner, other positions can be defined.

Table 2. Formation Energies for Different Vacancy Type Defect Configurations^a

defect type	$E_{\text{formation}}$ (eV)		figure	
	single	tetra	single	tetra
nonbonded	7.2	10.6		3g
FCC-top	4.3	8.8	3b	
FCC-hcp	5.5	6.8	3c	3e
HCP-top	4.2	8.5		
HCP-fcc	5.3	6.9		3f
TOP-hcp	4.8	≈ 12.7		
TOP-fcc	4.7	12.9	3d	

^aCapital letters denote the region, and the small ones stand for the position of the missing C atom (the central atom in the case of tetra-vacancies). Calculations using the VV10³⁶ vdW functional gave similar results; see Table 1 in the Supporting Information.

As evident from Table 2, for both single and tetra vacancies, the formation energy varies significantly with the position in the supercell. Single vacancies always prefer to be on top of an Ir atom. The interaction between C atoms with dangling bonds and Ir atoms is so strong that the underlying Ir atom is essentially pulled out. For the optimum positions, the energy is lower in the HCP/FCC regions, as compared to TOP regions. The reason for this is obvious from geometrical considerations: The dangling carbon bonds saturate by connecting with the metal surface underneath. Vacancy formation energy in the TOP regions is higher, as there is no good match between the underlying Ir atoms and the C atoms with dangling bonds. This saturation of dangling bonds also explains the funnel-like shape of the vacancies and fewer localized states close to the Fermi level. STM images of vacancies simulated using an approach based on the first-order surface-tip interaction perturbation theory³⁸ confirmed the funnel-like shape of such defects (cf. Figure S2 in Supporting Information). Also note that the formation energy of tetra vacancies is only slightly higher than for single vacancies, indicating that vacancies should cluster under heating.

This strongly varying potential energy landscape for vacancies opens a path for ion beam structuring of graphene on Ir(111): For the right combination of vacancy defect creation, migration, and annihilation it should be possible to enable vacancy relaxation within one moiré cell, while at the same time avoiding complete defect annealing by staying below the onset of intercell diffusion of vacancy agglomerates. Thereby one could create a graphene sheet with an ordered array of holes, constituting a graphene nanomesh at a 2.53 nm scale. The remainder of this Letter is devoted to the experimental realization of this structure.

For an ideal nanomesh, one vacancy aggregate has to be present in every single moiré cell. In addition, secondary effects like Ir sputtering have to be suppressed. These conditions can be met by reducing the ion energy ($E = 0.5$ keV) while at the same time increasing ion fluence substantially. The sample topography for $F = 0.02$ MLE and after annealing to 850 K is shown in Figure 4a. The holes are arranged in a partially occupied honeycomb lattice. We superimposed a hexagonal lattice associated with the TOP regions of the moiré. Therefore it is obvious that the holes are never located in the TOP regions but prefer the HCP/FCC regions, as predicted by our DFT calculation. The fraction of defective moiré cells amounts to $p \approx 0.3$.

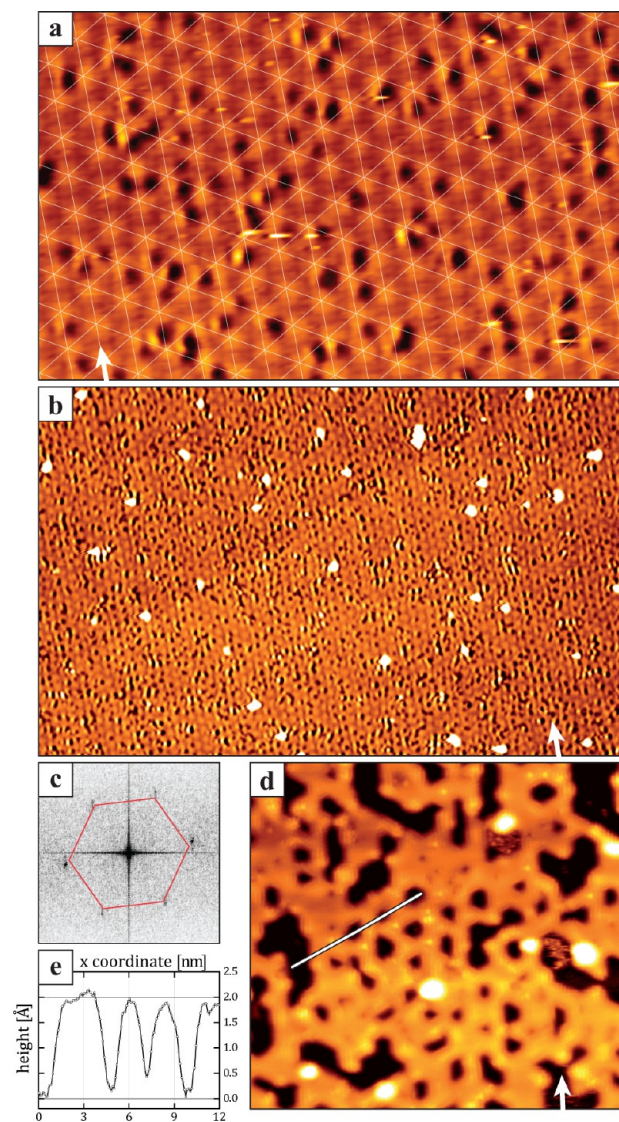


Figure 4. Graphene nanomesh. (a) Fully graphene covered Ir(111) surface (topographic contrast) after irradiation with 0.5 keV Xe⁺ ions at room temperature under 75° off normal, fluence $F = 0.02$ MLE, $T_{\text{anneal}} = 850$ K. The image shows a dense arrangement of defects in honeycomb order. A hexagonal lattice is superimposed. (b) Graphene nanomesh (topographic contrast) obtained by a further increased fluence $F = 0.05$ MLE. (c) Fourier transform of b, the hexagonal symmetry is highlighted, referring to a long-range defect ordering. The method to calculate this Fourier transform is documented in Figure S3. (d) Ordered lattice of larger vacancy clusters created by irradiation at 900 K using 0.05 MLE of 1 keV Xe⁺. (e) Height profile along the line indicated in d, from left to right. Arrows in a, b, and d are pointing along the direction of the impinging ions. Image width: (a) 40 nm, (b) 160 nm, (c) 1.5 nm⁻¹, (d) 27 nm; imaging parameters: (a,b) $I = 0.2$ nA, $U = 2.0$ V, (d) $I = 0.3$ nA, $U = 0.9$ V.

For further increased fluences $F = 0.05$ MLE (see Figure 4b), the defect pattern exhibits a denser arrangement, showing a single component in the Fourier transform (Figure 4c). The presence of sharp reflexes confirms that the positions of the holes are correlated. Note that the moiré, though faintly visible in the background with topographic contrast, was filtered out prior to applying the Fourier transform as documented in Figure S3. The topograph also shows some prominent protrusions which we interpret as carbon clusters buried at

the graphene/Ir interface. This assumption is accounted for by the annealing temperature sufficient for dissociation of iridium adatom clusters; see Figure 2, as well as the change of bombardment parameters: With a reduction of the ion energy to 0.5 keV Ir adatom production is drastically reduced,³⁹ and the dominating process in defect creation is the displacement of individual carbon atoms upon first impact, which come to rest in the interface. Increasing the energy of the ions to 1 keV and performing the irradiation at an elevated temperature of $T = 900$ K leads to the formation of larger vacancy clusters which start to take a hexagonal shape (see Figure 4d). The vacancies still follow the template of the moiré superlattice, but large parts of the iridium substrate are exposed. The height profile shown in Figure 4e shows a two-level system (thin horizontal lines). Note that the STM tip does not reach down to the substrate only in large vacancy islands, whereas the profiles of smaller defects are dominated by the finite size of the tip.

The above findings show that our method is able to produce a graphene nanomesh on a 2.53 nm scale. It is formed by relaxation of vacancies created by ion irradiation to the locations of minimal formation energy within one moiré unit cell, thereby lowering the total system energy substantially. Note that nanomesh formation can only take place in the narrow temperature window above the onset of relaxation within one moiré cell but below the activation of intercell vacancy migration. The structural order as well as the hole size of the nanomesh can be controlled by the process parameters of ion species, energy, angle, and the temperature treatment of the sample during and after irradiation.

In conclusion, our experiments on ion bombardment of graphene/Ir(111) show that interface channeling plays a key role in the defect creation mechanism at grazing incident ions, causing both carbon sputtering and iridium adatom production. The resulting graphene defects are thermally stable up to 900 K, whereas defects in the iridium substrate are already completely annealed at 700 K. All dangling carbon bonds are saturated by connecting to the metal surface, causing the vacancy structures to assume a funnel-like shape. Using the right process parameters, a regular pattern appears spontaneously due to an interplay of creation and thermally activated diffusion of vacancies. We were able to drive and confine the vacancies at the HCP/FCC regions of the moiré superstructure, thereby forming a hexagonal graphene nanomesh with a 2.53 nm periodicity, opening new possibilities for tailoring the mechanical and electronic properties of graphene.

■ ASSOCIATED CONTENT

Supporting Information

Further experimental analysis of the defect morphology, simulations of STM images of vacancies in the graphene layer on an Ir(111) support, results of DFT calculations with the VV10 functional, and details on the calculation of the Fourier Transform shown in Figure 4. This material is available free of charge via the Internet at <http://pubs.acs.org>.

■ AUTHOR INFORMATION

Corresponding Author

*E-mail: standop@ph2.uni-koeln.de.

Notes

The authors declare no competing financial interest.

■ ACKNOWLEDGMENTS

We acknowledge experimental help with the STS experiments by S. Runte and J. Klinkhammer. The authors acknowledge financial support from the European Commission via the seventh Framework Program project “Graphene for Nano-scaled Applications (GRENADA)”, the Bonn-Cologne Graduate School of Physics and Astronomy, the DFG through SFB 608 and INST 2156/514-1, and the Finnish Cultural Foundation. We also thank the Academy of Finland for the support through projects 218545 and 263416, as well as the University of Helsinki Funds. Generous grants of computer time provided by CSC Finland are also acknowledged.

■ REFERENCES

- (1) Chan, W. L.; Chason, E. *J. Appl. Phys.* **2007**, *101*, 121301.
- (2) Facsko, S.; Dekorsy, T.; Koerdt, C.; Trappe, C.; Kurz, H.; Vogt, A.; Hartnagel, H. *Science* **1999**, *285*, 1551–1553.
- (3) Krasheninnikov, A. V.; Banhart, F. *Nat. Mater.* **2007**, *6*, 723–733.
- (4) Krasheninnikov, A. V.; Nordlund, K. *J. Appl. Phys.* **2010**, *107*, 071301.
- (5) Fernandez-Rossier, J.; Palacios, J. J. *Phys. Rev. Lett.* **2007**, *99*, 177204.
- (6) Cai, J.; Ruffieux, P.; Jaafar, R.; Bieri, M.; Braun, T.; Blankenburg, S.; Muoth, M.; Seitsonen, A. P.; Saleh, M.; Feng, X.; Müllen, K.; Fasel, R. *Nature* **2010**, *466*, 470–473.
- (7) Bai, J.; Zhong, X.; Jiang, S.; Huang, Y.; Duan, X. *Nat. Nanotechnol.* **2010**, *5*, 190–194.
- (8) Fürst, J. A.; Pedersen, J. G.; Flindt, C.; Mortensen, N. A.; Brandbyge, M.; Pedersen, T. G.; Jauho, A.-P. *New J. Phys.* **2009**, *11*, 095020.
- (9) Gunst, T.; Markussen, T.; Jauho, A.-P.; Brandbyge, M. *Phys. Rev. B* **2011**, *84*, 155449.
- (10) Yang, H.-X.; Chshiev, M.; Boukhalov, D. W.; Waintal, X.; Roche, S. *Phys. Rev. B* **2011**, *84*, 214404.
- (11) Zeng, Z.; Huang, X.; Yin, Z.; Li, H.; Chen, Y.; Li, H.; Zhang, Q.; Ma, J.; Boey, F.; Zhang, H. *Adv. Mater.* **2012**, *24*, 4138–4142.
- (12) Lemme, M. C.; Bell, D. C.; Williams, J. R.; Stern, L. A.; Baugher, B. W. H.; Jarillo-Herrero, P.; Marcus, C. M. *ACS Nano* **2009**, *3*, 2674–2676.
- (13) Akcöltekin, S.; Bukowska, H.; Peters, T.; Osmani, O.; Monnet, I.; Alzahr, I.; d’Etat, B. B.; Lebius, H.; Schleberger, M. *Appl. Phys. Lett.* **2011**, *98*, 103103.
- (14) Kotakoski, J.; Krasheninnikov, A. V.; Kaiser, U.; Meyer, J. C. *Phys. Rev. Lett.* **2011**, *106*, 105505.
- (15) Warner, J. H.; Margine, E. R.; Mukai, M.; Robertson, A. W.; Giustino, F.; Kirkland, A. I. *Science* **2012**, *337*, 209–212.
- (16) Ugeda, M. M.; Brihuega, I.; Guinea, F.; Gómez-Rodríguez, J. M. *Phys. Rev. Lett.* **2010**, *104*, 096804.
- (17) Ugeda, M. M.; Fernández-Torre, D.; Brihuega, I.; Pou, P.; Martínez-Galera, A. J.; Pérez, R.; Gómez-Rodríguez, J. M. *Phys. Rev. Lett.* **2011**, *107*, 116803.
- (18) Ugeda, M. M.; Brihuega, I.; Hiebel, F.; Mallet, P.; Veuillen, J.-Y.; Gómez-Rodríguez, J. M.; Ynduráin, F. *Phys. Rev. B* **2012**, *85*, 121402.
- (19) van Gastel, R.; N’Diaye, A. T.; Wall, D.; Coraux, J.; Busse, C.; Buckanie, N. M.; Meyer zu Heringdorf, F.-J.; Horn-von Hoegen, M.; Michely, T.; Poelsema, B. *Appl. Phys. Lett.* **2009**, *95*, 121901.
- (20) Lehtinen, O.; Kotakoski, J.; Krasheninnikov, A. V.; Tolvanen, A.; Nordlund, K.; Keinonen, J. *Phys. Rev. B* **2010**, *81*, 153401.
- (21) Lehtinen, O.; Kotakoski, J.; Krasheninnikov, A. V.; Keinonen, J. *Nanotechnology* **2011**, *22*, 175306.
- (22) Horcas, I.; Fernandez, R.; Gomez-Rodríguez, J. M.; Colchero, J.; Gomez-Herrero, J.; Baro, A. M. *Rev. Sci. Instrum.* **2007**, *78*, 013705.
- (23) N’Diaye, A. T.; Bleikamp, S.; Feibelman, P. J.; Michely, T. *Phys. Rev. Lett.* **2006**, *97*, 215501.
- (24) Busse, C.; Lazić, P.; Djemour, R.; Coraux, J.; Gerber, T.; Atodiresei, N.; Caciuc, V.; Brako, R.; N’Diaye, A. T.; Blügel, S.; Zegenhagen, J.; Michely, T. *Phys. Rev. Lett.* **2011**, *107*, 036101.

- (25) N'Diaye, A. T.; Coraux, J.; Plasa, T. N.; Busse, C.; Michely, T. *New J. Phys.* **2008**, *10*, 043033.
- (26) Standop, S.; Lehtinen, O.; Lewes-Malandrakis, G.; Herbig, C.; Michely, T.; Krasheninnikov, A. V.; Busse, C., to be published.
- (27) Nordlund, K.; Ghaly, M.; Averbach, R.; Caturla, M.; de la Rubia, T.; Tarus, J. *Phys. Rev. B* **1998**, *57*, 7556–7570.
- (28) Albe, K.; Nordlund, K.; Averbach, R. *Phys. Rev. B* **2002**, *65*, 195124.
- (29) Ziegler, J. F.; Ziegler, M. D.; Biersack, J. P. *Nucl. Instrum. Methods Phys. Res., Sect. B* **2010**, *268*, 1818–1823.
- (30) Kimura, K.; Hasegawa, M.; Mannami, M. *Phys. Rev. B* **1987**, *36*, 7–12.
- (31) Redinger, A.; Standop, S.; Michely, T.; Rosandi, Y.; Urbassek, H. *M. Phys. Rev. Lett.* **2010**, *104*, 075501.
- (32) Coraux, J.; N'Diaye, A. T.; Engler, M.; Busse, C.; Wall, D.; Buckanie, N.; Meyer zu Heringdorf, F.-J.; van Gastel, R.; Poelsema, B.; Michely, T. *New J. Phys.* **2009**, *11*, 023006.
- (33) Wang, S. C.; Ehrlich, G. *Surf. Sci.* **1990**, *239*, 301–332.
- (34) Kresse, G.; Furthmüller, J. *Phys. Rev. B* **1996**, *54*, 11169–11186.
- (35) Blochl, P. E. *Phys. Rev. B* **1994**, *50*, 17953–17979.
- (36) Vydrov, O. A.; Van Voorhis, T. *J. Chem. Phys.* **2010**, *133*, 244103.
- (37) Björkman, T. *Phys. Rev. B* **2012**, *86*, 165109.
- (38) Krasheninnikov, A. *Solid State Commun.* **2001**, *118*, 361–365.
- (39) Redinger, A.; Standop, S.; Rosandi, Y.; Urbassek, H. M.; Michely, T. *New J. Phys.* **2011**, *13*, 013002.